https://doi.org/10.5194/egusphere-2026-727
Preprint. Discussion started: 23 February 2026

Leveraging Machine Learning techniques and SEVIRI data to detect volcanic clouds composed of ash, ice, and SO_2

Camilo Naranjo[1], Lorenzo Guerrieri[1], Stefano Corradini[1], Matteo Picchiani[2], Luca Merucci[1] and Dario Stelitano[1]

[1]INGV, Istituto Nazionale di Geofisica e Vulcanologia, ONT, 00143 Rome, Italy
[2]ASI, Italian Space Agency, 00133 Rome, Italy

Correspondence to: Camilo Naranjo (camilo.naranjo@ingv.it)

Abstract. Volcanic clouds can influence the climate and pose a serious threat to air transportation. Detecting and distinguishing them from meteorological clouds is particularly challenging because they often are composed of water vapor and ice particles, along with ash and gases. This study presents a Neural Network (NN) model for the detection of volcanic clouds composed of ash, ice, and SO_2, applied to data acquired by the Spinning Enhanced Visible and InfraRed Imager (SEVIRI) satellite instrument. A dataset of 1.259 SEVIRI images related to Etna volcano eruptions spanning from 2020 to 2022, as well as 2024, was considered. The NN model, based on a multi-layer perceptron (MLP), was developed using 13 features, including thermal infrared channels and brightness temperature differences (BTD's). The model was validated on three eruptive events not used in the training phase, demonstrating an overall high accuracy of 99%, a precision >89%, a recall >74% and excellent capability to detect volcanic clouds, even in complex scenarios of high meteorological cloud cover. The results are promising for automatic and near-real-time detection of volcanic clouds, including those containing ice, and for improving retrieval processes.

1. Introduction

Volcanic eruptions can release vast amounts of ash particles and gases into the atmosphere and form volcanic clouds that pose serious risks to aviation (Alexander, 2013; Prata and Rose, 2015), to human health (Stewart et al., 2021), to the environment and the climate (Jenkins et al., 2023; Marshall et al., 2022). Detecting volcanic clouds is crucial for aviation safety and assessing their potential impact, for height estimation methods, retrieval algorithms, and dispersion models. Nonetheless, the detection of volcanic clouds continues to pose a significant challenge (Prata et al., 2022).

The use of satellite imagery has been essential for advancing volcanic cloud detection capabilities, as they can collect information over large areas and across a broad range of wavelengths. The widely recognized method for detecting volcanic clouds containing ash is the Brightness Temperature Difference (BTD) technique, based on the difference between the channels centered around 11 and 12 µm, which was postulated by Prata (1989a, 1989b). It exploits the reverse absorption phenomenon that occurs in the 11 µm and 12 µm wavelengths range. In this spectral region, the volcanic ash signature is opposite to that of water and ice, which are the primary components of meteorological clouds. Specifically, ash absorbs more energy around the

https://doi.org/10.5194/egusphere-2026-727
Preprint. Discussion started: 23 February 2026

11 µm band, whereas water and ice absorb more energy around the 12 µm band. As a result, the BTD is normally negative in the presence of ash and positive in the presence of meteorological clouds. However, there are some well-known circumstances in which the BTD method fails, leading to false positives and false negatives during the detection (Pardini et al., 2024; Prata et al., 2001). Over the last two decades, many studies have focused on improving and overcoming the limitations of the BTD method by presenting more sophisticated approaches, such as water vapor correction (Corradini et al., 2008; Yu et al., 2002), methods using multiple channels for daytime detection (Ellrod et al., 2003; Pavolonis et al., 2006; Pergola et al., 2004), principal component analysis (Hillger and Clark, 2002), β ratios (Pavolonis et al., 2015a, b), and machine learning techniques (Gray and Bennartz, 2015; Petracca et al., 2022; Picchiani et al., 2011, 2015; Piscini et al., 2014; Romeo et al., 2023; Torrisi et al., 2022, 2024).

Despite all these approaches, there is still a need for reliable methods that can automatically detect volcanic clouds, particularly when they contain a mixture of ash, ice, and SO_2. The detection of SO_2 in volcanic clouds can be effectively achieved using the 7.3 µm and 8.6 µm wavelength bands, where SO_2 exhibits strong absorption features. Although the 7.3 µm band shows stronger absorption, it is also influenced by significant water vapor interference (Corradini et al., 2009; Pavolonis et al., 2020). Thus, by combining data from both bands, it is possible to enhance the reliability of SO_2 detection.

Moreover, the presence of ice in volcanic clouds is tricky, as it masks the spectral response of ash (Rose et al., 1995). Since ice has an opposite spectral response to ash, it produces a positive BTD for volcanic clouds when present, resulting in false negatives and complicating the accurate detection of volcanic clouds (Guerrieri et al., 2023; Gupta et al., 2022; Mayberry et al., 2002; Prata et al., 2020; Rose et al., 1995, 2003). False negatives in detection are caused by ice formation through nucleation processes occurring within volcanic clouds (Durant et al., 2008), which can be either homogeneous (Prata et al., 2020) or heterogeneous (Seifert et al., 2011). In the latter case, volcanic ash particles act as ice nuclei (Wang, 2013).

The limited understanding of nucleation processes within volcanic clouds underlines the need for accurate detection methods in these circumstances (Durant et al., 2008; Schill et al., 2015). This need aligns with the requirements of the International Civil Aviation Organization (ICAO), which expects all Volcanic Ash Advisory Centers (VAACs) to provide Quantitative Volcanic Ash (QVA) information by late 2027 (ICAO, 2021, 2024). However, obtaining accurate QVA information relies, though not exclusively, on precise detection methods (Guerrieri et al., 2023; Prata et al., 2022).

With the purpose of exploring the detection of volcanic clouds containing a mixture of ash, ice, and SO_2, this paper focuses on leveraging Machine Learning techniques and data from the Spinning Enhanced Visible and InfraRed Imager (SEVIRI) instrument aboard the Meteosat Second Generation (MSG) geostationary satellite. As a case study, the eruptive activity of Mount Etna (Italy) was analysed for the periods 2020–2022 and 2024, where the events generated volcanic clouds with varying combinations of constituents (Guerrieri et al., 2023), offering a unique opportunity to investigate the detection challenge. The results provide insights into the detection of ash, ice, and SO_2 within volcanic clouds and show promise for the automatic detection and retrieval of volcanic clouds in near-real time.

https://doi.org/10.5194/egusphere-2026-727
Preprint. Discussion started: 23 February 2026

This paper is organised as follows: Section 2 describes the case study, the SEVIRI satellite instrument characteristics and how the training dataset was built. Section 3 covers the development of the NN model and the different steps involved. The results are presented in Section 4 and the discussion in Section 5. Final conclusions are drawn in Section 6.

2. Materials and methods

This section presents a description of the case study, the SEVIRI data and how the training dataset was built.

2.1. Case study

As a case study, the Etna eruption activity between 13 December 2020 and 21 February 2022 was selected. During this period, Etna volcano produced 66 lava fountain episodes from the new South-East crater. Despite their short duration (an average time of about two hours (Calvari and Nunnari, 2022)), they produced a strong impact on human life, environment, and air traffic. These paroxysmal events produced large Volcanic Clouds Top Heights (VCTH) ranging from 4 to 13 km asl. Based on VCTH, the entire period can be approximately divided into three main time ranges characterized by average VCTH values of 9 km (from 13 December 2020 to 19 March 2021), 6 km (from 24 March 2021 to 17 June 2021) and 10 km (from 19 June 2021 to 21 February 2022). Most of these volcanic clouds were composed of ash, ice, and SO_2, with the ice content being greater than the ash. The ice generation was related not only to the volcanic cloud height but also to the season: during the summer, with almost the same plume height, the amount of ice was lower than that observed in winter (Guerrieri et al., 2023). The presence of ice in most volcanic clouds during this period makes it an interesting case study for exploring the challenges associated with volcanic cloud detection.

2.2. Satellite data

Data from the Spinning Enhanced Visible and InfraRed Imager (SEVIRI) instrument aboard the Meteosat Second Generation (MSG) geostationary satellite, specifically from the Meteosat-10 series orbiting at a 0 degrees longitude, was considered in this work. SEVIRI instrument can produce an image of the Earth's full disk every 15 minutes in 12 different spectral channels ranging from visible to infrared, with a nominal spatial resolution of 3x3 km^2 (1 km^2 for High-Resolution Visible channel) at the sub-satellite point (EUMETSAT, 2017). The SEVIRI's channel description and their nominal centre wavelengths are shown in Table 1. All the SEVIRI data used in this work was acquired in near real-time using the Multimission Acquisition SysTem (MAST), which was developed at Istituto Nazionale di Geofisica e Vulcanologia - Osservatorio Nazionale Terremoti (INGV-ONT). The MAST system uses EUMETCast dissemination service for the near real-time delivery of satellite data and products (Stelitano et al., 2023).

An example of a volcanic cloud captured by SEVIRI from 19 February 2021 at 10:15 UTC is displayed in Figure 1. This volcanic cloud is composed of a mixture of ash, ice, and SO_2. The natural color composite, which use the visible channels, is

https://doi.org/10.5194/egusphere-2026-727
Preprint. Discussion started: 23 February 2026

shown in Figure 1(a), where the volcanic cloud appears as a bright white cloud, similar to the surrounding meteorological clouds. By contrast, the volcanic cloud shown in Figure 1(b) is well distinguished in the Ash RGB composite, which uses the thermal infrared channel. In this latter figure, generated by combining the thermal infrared channels centered at 8.7, 10.8 and 12.0 µm (Ash RGB Quick Guide | EUMETSAT - User Portal, 2025), the volcanic cloud constituents are clearly identifiable: ash appears in shades of brown, ice in dark blue, and SO_2 in green color.

Table 1. Spectral channels description of the Spinning Enhanced Visible and InfraRed Imager (SEVIRI) instrument.

Channel ID	Channel Description	Nominal Centre Wavelength (µm)	Spectral Bandwidth (µm)
HRV	Visible High Resolution	0.75	0.6 to 0.9
VIS 0.6	Visible	0.635	0.56 to 0.71
VIS 0.8	Near-Infrared	0.81	0.74 to 0.88
IR 1.6	Near-Infrared	1.64	1.50 to 1.78
IR 3.9	Near-Infrared with reflected daytime component	3.92	3.48 to 4.36
IR 6.2	Upper-Level Tropospheric Water Vapor	6.25	5.35 to 7.15
IR 7.3	Lower-level Water Vapor	7.35	6.85 to 7.85
IR 8.7	Sulphur dioxide (SO_2) / Infrared window	8.70	8.30 to 9.10
IR 9.7	Ozone	9.66	9.38 to 9.94
IR 10.8	Infrared window	10.80	9.80 to 11.80
IR 12.0	Infrared window	12.00	11.00 to 13.00
IR 13.4	Carbon Dioxide (CO_2)	13.40	12.40 to 14.40

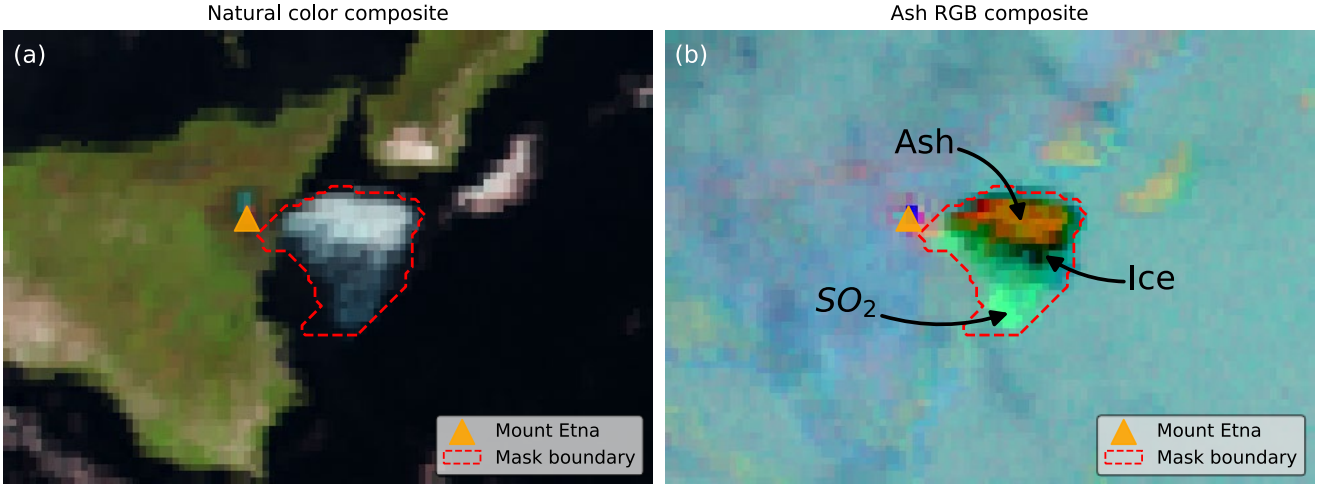

Figure 1. A volcanic cloud containing a mixture of ash, ice, and SO_2 on 19 February 2021 at 10:15 UTC, captured by SEVIRI-MSG. (a) Natural color composite with an overlaid hand-drawn volcanic cloud boundary. (b) Same as (a) but showing the ash RGB composite. The cloud's regions where ash, ice, and SO_2 are present have been highlighted with a mask boundary.

https://doi.org/10.5194/egusphere-2026-727
Preprint. Discussion started: 23 February 2026

2.3. Dataset

The dataset was generated from 1.259 SEVIRI images covering 49 eruptive Etna events between December 2020 and February 2022 (see Figure 2.1). Table S1 provides a detailed description of the SEVIRI images employed to generate the dataset, including the number of images and the time range for each event. All images were manually analysed in order to create a plume mask for each one; this step, generally known as the labelling process (see Figure 2.2), was also used in Guerrieri et al. (2023) to estimate the total masses of ash, ice, and SO_2. The manual plume mask generation provides the most precise detection, but it requires an expert operator and is time-consuming. Figure 1 also presents an example of a plume mask.

In this work, the detection of volcanic cloud using SEVIRI data is analysed as a pixel-scale classification (see Figure 2.2(iii)). Thus, the dataset includes information from more than 2.200.000 pixels, organized in two balanced classes: 50% belonging to the Volcanic Cloud class (VC) and the other 50% to the Non-Volcanic Cloud class (NVC), as indicated in Figure 2.3. The original dataset was highly imbalanced, containing 0.3% VC pixels and 99.7% NVCC pixels. All VC pixels were retained, while NVC pixels were randomly sampled to obtain the final balanced dataset.

Among the pixel features that comprise the dataset are the thermal radiances from seven spectral channels, corresponding to the thermal-infrared region (6 – 14 μm) as detailed in Table 1. Selecting these spectral channels enhances model flexibility, allowing application both during the day and at night with a unique NN model. In the dataset, the thermal radiance from each channel is expressed as Brightness Temperature (BT) in Kelvin (K).

In addition, several channel combinations were applied to derive six new features, known in the literature as Brightness Temperature Difference (BTD) including the traditional BTD between the channels centered around 11 and 12 μm. These new features are: BTD[10.8-12.0], BTD[10.8-8.7], BTD[10.8-13.4], BTD[10.8-6.2], BTD[10.8-7.3] and BTD[10.8-9.7].

Thus, a total of 13 features are included in the dataset (as indicated in Figure 2.1), all serving as input variables for the neural network model.

3. Model development

This section presents the development of the neural network model including the parameterization, training and validation phases.

Using the previously built training dataset a Neural Network (NN) model based on a multi-layer perceptron (MLP) with a feed-forward architecture was implemented to perform the detection of volcanic clouds. This architecture was chosen due to its efficiency in handling large volumes of data with both accuracy and speed, as well as its ability to incorporate a priori knowledge and realistic physical constraints into the analysis (Atkinson and Tatnall, 1997). Further details of the Neural Network model are provided in the following subsections.

https://doi.org/10.5194/egusphere-2026-727
Preprint. Discussion started: 23 February 2026

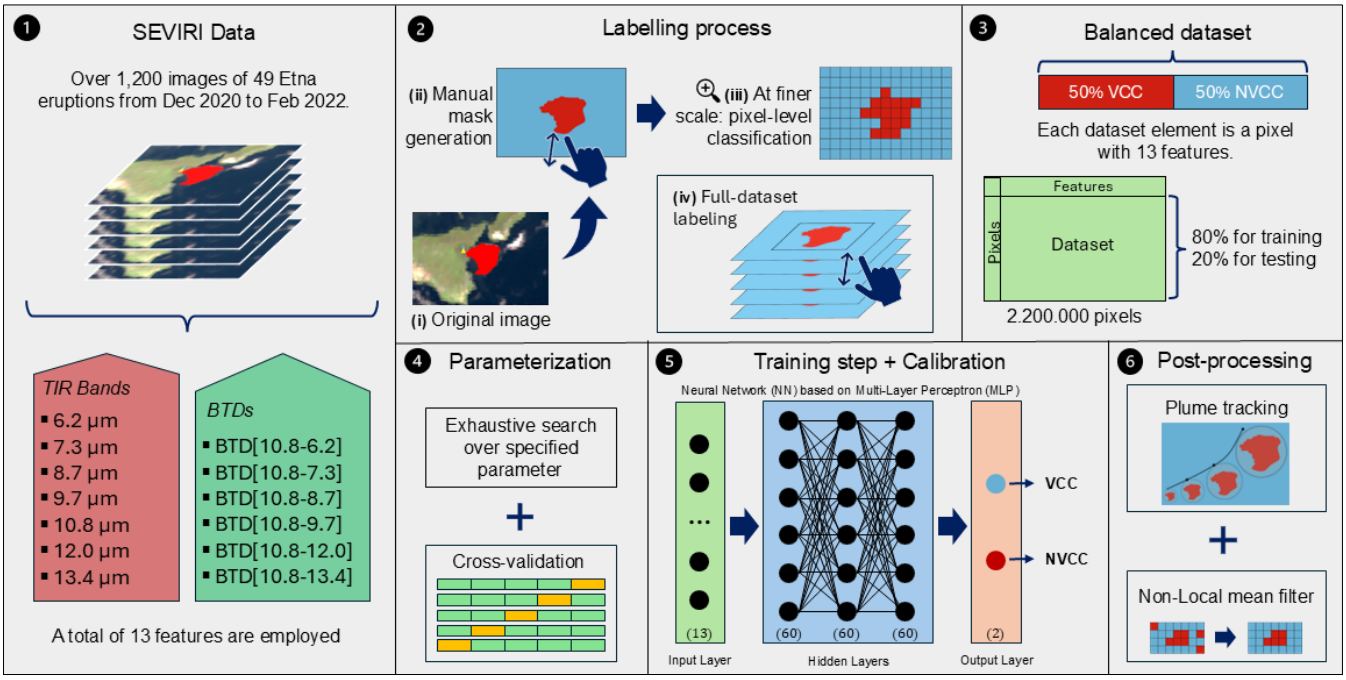

* VCC = Volcanic Cloud Class. NVCC = Non-Volcanic Cloud Class.

Figure 2. Model development overview. 1) SEVIRI data and features information. 2) Labelling workflow. 3) Dataset composition and division. 4) Parameterization. 5) Training. 6) Postprocessing.

3.1. Parameterization

A parameter optimization step was carried out to determine the most suitable configuration for the NN model. During this step, the parameters listed in Table 2 were optimized using the search space specified in the table's right column. This process combined exhaustive search with a 5-fold cross-validation strategy (k = 5) (Ojala and Garriga, 2010), evaluating all possible combinations within the defined optimization space. Moreover, the dataset was split into 80% for the training set and 20% for the test set.

To select the most suitable parameter configuration, both accuracy and the average time required for the Neural Network to perform an individual classification were considered. The final selected parameters can be found in Table 3 (section 3.2 Training phase).

Table 2. List of parameters and optimization space used in the parameterization step.

Parameter	Optimization space
Number of hidden layers	1, 2, 3, 5, 6, 8, 10, 15
Neurons for each hidden layer	10, 15, 20, 50, 60, 80, 100
Learning rate	$1 \times 10^{-3}, 1 \times 10^{-2}, 1 \times 10^{-1}$
L2 regularization	$1 \times 10^{-3}, 1 \times 10^{-2}, 1 \times 10^{-1}$

https://doi.org/10.5194/egusphere-2026-727
Preprint. Discussion started: 23 February 2026

3.2. Training phase

During the training phase, the dataset was also split into 80% for the training set and 20% for the test set, as in the parameterization step. Additionally, the data were standardized by removing the mean and scaling to unit variance. The NN model was trained using three hidden layers, each containing 60 neurons, as presented in Table 3. The learning rate and L2 regularization parameter were both set to 1×10^{-3}. The activation function used was a Rectified Linear Unit (ReLU) (Braga-Neto, 2020; Yang, 2019), and the Adam algorithm was employed for weight optimization (Kingma and Ba, 2014). Finally, the maximum number of training iterations was set to 300 and an early stopping strategy was applied.

In addition, the NN model was calibrated so that the predicted class probabilities correspond to the distribution of the observed pixels in the dataset. In this way, the probabilities can be interpreted as the model's confidence that each pixel belongs to a specific class label (Bröcker and Smith, 2007). The calibration plot for the trained NN model is shown in Figure 3a, where the y axis represents the observed proportion of VC class elements in the dataset, whereas the x axis represents the predicted probabilities for these elements.

As shown in Figure 3a, the NN model exhibits a slight tendency to overestimate low probabilities and underestimate high probabilities. However, the overall calibration performance is good, as can be seen in Figure 3b. This figure presents the distribution of predicted probabilities, showing that for the VC class, most probabilities are concentrated at low (less than 0.2) and high (greater than 0.8) values. This symmetric and bimodal distribution indicates that only a small number of ambiguous probability values are present, which is a desirable characteristic of a well-calibrated classifier.

Table 3. Values of the parameters used to train the final Neural Network model.

Parameter	Value
Number of hidden layers	3
Neurons for each hidden layer	60
Learning rate	1×10^{-3}
L2 regularization	1×10^{-3}
Activation function	ReLu
Optimization algorithm	Adam
Maximum number of iterations	300

https://doi.org/10.5194/egusphere-2026-727
Preprint. Discussion started: 23 February 2026

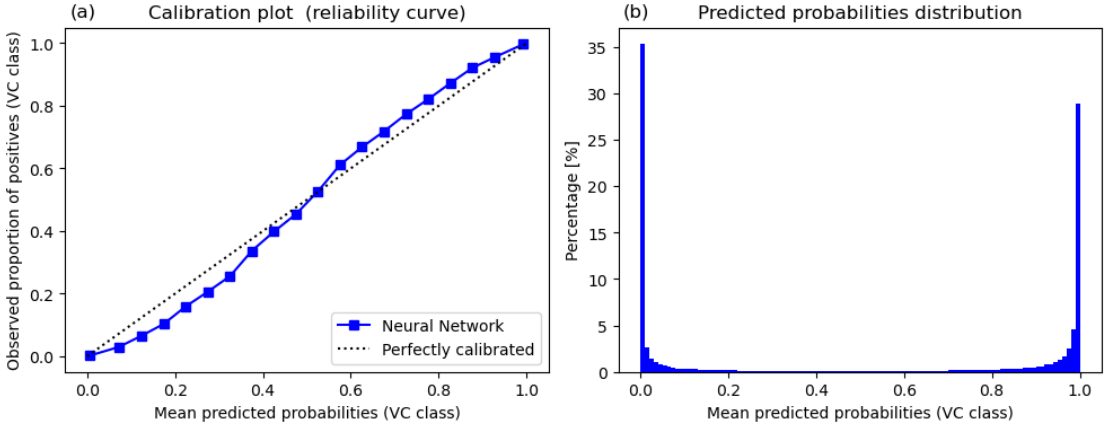

Figure 3. Reliability curve for the calibrated trained model.

175

3.3. Validation

To validate the performance of the NN model, three sequences of SEVIRI images were selected, each corresponding to an eruption the model had not previously encountered during the training phase. The events are listed in Table 4, comprising two from 2021 and one from 2024. The SEVIRI images for the 2024 event were captured by the Meteosat-11 satellite. In contrast,
180 the images for the 2021 events were captured by the Meteosat-10 satellite, the same satellite used to acquire the data for the training phase. All three events represent challenging scenarios in which the volcanic clouds are composed of ash, ice, and SO_2.

Each SEVIRI image sequence was also manually analysed to create a plume mask for each image, following the same labelling process carried out for the training dataset (as illustrated in Figure 2.2). The plume masks are used as ground truth to compare
185 the predictions of the NN model and assess its performance through conventional evaluation metrics such as accuracy, precision, recall, F1-score and confusion matrix (Fawcett, 2006; Rainio et al., 2024).

Table 4. List of events and SEVIRI images used to the validation.

Event ID	Number of SEVIRI images	Start date and time (UTC)	End date and time (UTC)
1	30	22 Feb 2021, 23:00	23 Feb 2021, 06:30
2	47	4 Mar 2021, 07:30	4 Mar 2021, 19:00
3	25	4 Aug 2024, 03:00	4 Aug 2024, 09:00

3.4. Plume tracking and non-local mean filter

190 The raw output of the NN model is subsequently post-processed using a plume tracking method and a non-local (NL) mean filter. This two-step post-processing procedure is designed to reduce false positive detections (see Figure 2.6). A similar methodology was previously presented by Pavolonis et al. (2018), who introduced the Cloud Growth Anomaly (CGA) technique.

https://doi.org/10.5194/egusphere-2026-727
Preprint. Discussion started: 23 February 2026

The tracking algorithm developed in this work is initialized (t_0) within an area corresponding to a 25 km radius around the Etna volcano, as depicted in Figure 4(a). Pixels falling outside this region are not considered in the analysis. It is important to note that the processing is performed in image coordinates (x, y pixel coordinates). Therefore, this area corresponds to selecting the pixels located within a circular region of approximately 8 pixels in radius, given that SEVIRI data has a spatial resolution of 3 km per pixel.

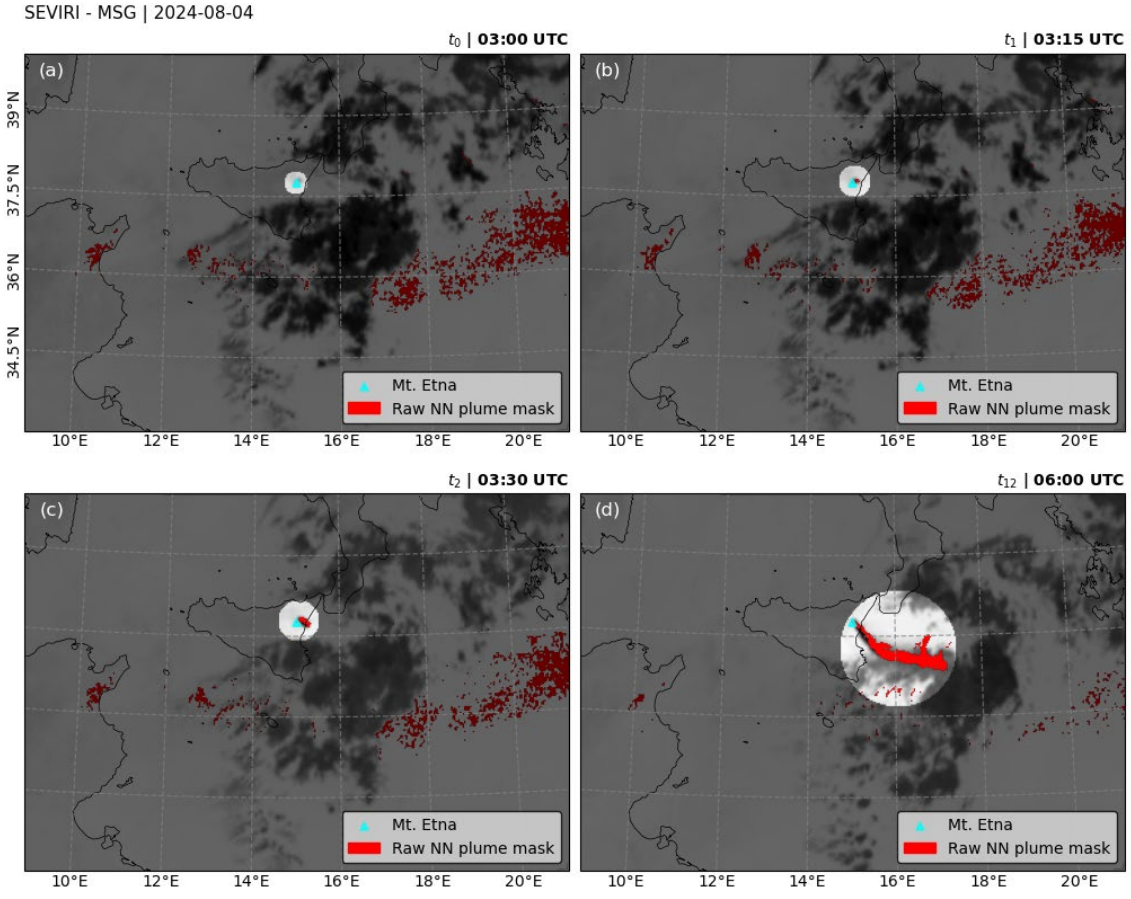

Figure 4. Example of plume tracking from the 4 August 2024 eruption of the Mount Etna. (a) At t_0 = 03:00 UTC, a volcanic cloud (VC) object was not yet detected within the 25 km radius around the volcano. (b) At t_1 = 03:15 UTC, the first VC object is detected, which is the triggering event. (c) At t_2 = 03:30 UTC. (d) At t_{12} = 06:00 UTC, the dispersed VC tracked by the algorithm.

At first, the algorithm evaluates every new prediction from the NN model, searching for pixels classified as volcanic cloud (VC), which serve as the triggering event. The raw NN plume mask is treated as a potential VC object. When such a VC object appears within the area of interest, the tracking algorithm initiates tracking at time $t_{i=1}$ and proceeds to analyse the subsequent images. Thus, in the subsequent images, two processes occur:

https://doi.org/10.5194/egusphere-2026-727
Preprint. Discussion started: 23 February 2026

- The radius of the circular region increases by approximately 9-15 km (3-5 pixels) for each new image (t_{i+1}), depending on the wind speed for that day. These values are based on typical wind speeds of 10–16 m/s and the SEVIRI spatial resolution.
- The center of the circular region is updated for the next image (t_{i+1}) to the centroid of the previously detected VC object. This allows the algorithm to fully track the VC object over time.

This operation continues until no pixels from the raw NN plume mask remain within the tracking area. Figure 4 shows an example of the plume tracking algorithm in action.

At each iteration (i) of the tracking algorithm, outlier pixels are removed using a non-local (NL) mean filter (Buades et al., 2005), after which a binary dilation filter is applied. The algorithm is also robust in tracking fragmented volcanic clouds, as shown in Figure 5e in the Results section.

Finally, the final results and performance metrics presented in the results section correspond to the data obtained after applying this step.

3.5. Explainability method

As outlined in the subsection 3.2, the NN model consists of three hidden layers with 60 neurons each one and uses 13 input features, resulting in a complex model. This level of complexity limits the understandability of the model's classification process (Flora et al., 2024). In order to better understand the classification process, an explainability method called Shapley Additive Explanations (SHAP) was used. SHAP values is a game-theoretic framework that quantifies the contribution of each feature to individual predictions, thereby providing insight into the model's overall internal mechanisms (Lundberg et al., 2017). The discussion section presents a beeswarm plot illustrating feature relevance for the NN model based on the training dataset.

4. Results

As outlined in the introduction, the presence of ice within volcanic clouds poses a limitation for an accurate detection. This challenge was recently reviewed by Pardini et al. (2024) and has also been discussed by several other authors in the past (Durant et al., 2008; Prata et al., 2020; Rose et al., 1995). To address this detection challenge, the main objective of this study was to explore the performance of a NN model in detecting volcanic clouds composed of a mixture of ash, ice, and SO_2, using a comprehensive dataset from the SEVIRI sensor, in order to automatically detect volcanic clouds and subsequently retrieve their mass loading information. In this context, the NN model trained for this challenging task was validated using the manual plume masks as reference. The three validation events are listed in Table 4.

This section presents the detection results for these events, which are summarized in Table 5. The metrics reveal that the overall accuracy for all validation events reached 0.99, indicating that 99% of the pixels were correctly classified throughout the entire sequence of each event. The following subsections present the results for each event, followed by a metrics analysis.

https://doi.org/10.5194/egusphere-2026-727
Preprint. Discussion started: 23 February 2026

Table 5. Performance metrics for the three validation events.

Event	Accuracy	Precision	Recall	F1-Score
1: 22 Feb 2021	0.9938	0.9590	0.8293	0.8832
2: 4 Mar 2021	0.9973	0.9788	0.7424	0.8216
3: 4 Aug 2024	0.9955	0.8897	0.9196	0.9041

4.1. Event 1: 22-23 Feb 2021

This event was a paroxysmal episode at the Southeast Crater, which lasted 10 hours. It was primarily characterized by a lava fountain with a duration of 50 minutes and a volcanic cloud that reached more than 11 km in height (Guerrieri et al., 2023; INGV, 2021b).

At the onset of this event, the volcanic cloud was dispersed toward the northwest, and it is observed with a thick core displaying brown shades, indicating a high concentration of particles, presumably ash. In contrast, the cloud's edges appear in dark blue tones, suggesting thinner regions primarily composed of ice (see Figure 5b). As the eruption progresses, the denser portion of the cloud disperses and eventually appears entirely dark blue, highlighting a strong presence of ice. Additionally, a sulphur dioxide (SO_2) signal is visible in the northern part of the cloud, represented in green tones (see Figure 5d). By the end of the sequence, the primary volcanic cloud has dissipated, and a new eruptive pulse produces a low-level volcanic cloud, visible in red shades in Figure 5f.

Notably, in Figure 5a, 5c, and 5e, the NN model effectively detects most components and the overall structure of the volcanic cloud throughout its evolution, even when the cloud becomes fragmented as is revealed in Figure 5e. The metrics of precision, recall and F1-score for this event were 0.96, 0.83 and 0.88, respectively, as reported in Table 5.

4.2. Event 2: 04 Mar 2021

This second event was produced by a strombolian activity at the Southeast Crater, which started at 7:50 UTC. The activity then evolved into a lava fountain that generated a volcanic cloud rising to more than 11 km (Guerrieri et al., 2023; INGV, 2021a).

For this event, the evolution of the volcanic cloud is quite similar to the previous case. In this instance, the cloud moves toward the northeast. At the onset, ash particles are observed in the inner part of the cloud, shown in brown shades (see Figure 6b), which are later masked by ice (see Figure 6d). Additionally, the SO_2 signal, visible in green, becomes more prominent toward the end of the sequence.

Unlike the previous case, this volcanic cloud remains compact, and the NN model successfully detects most parts of the cloud throughout the sequence (see Figure 6a, 6c, and 6e). The cloud was continuously tracked for 12 hours and over a distance exceeding 550 km from the volcano. Toward the end of the sequence, some portions of the volcanic cloud containing SO_2 are no longer detected, as illustrated in Figure 6f. The reduced detection performance is likely attributable to cloud dilution in those areas, resulting in lower recall and F1-score values of 0.74 and 0.82, respectively, as reported in Table 5.

https://doi.org/10.5194/egusphere-2026-727
Preprint. Discussion started: 23 February 2026

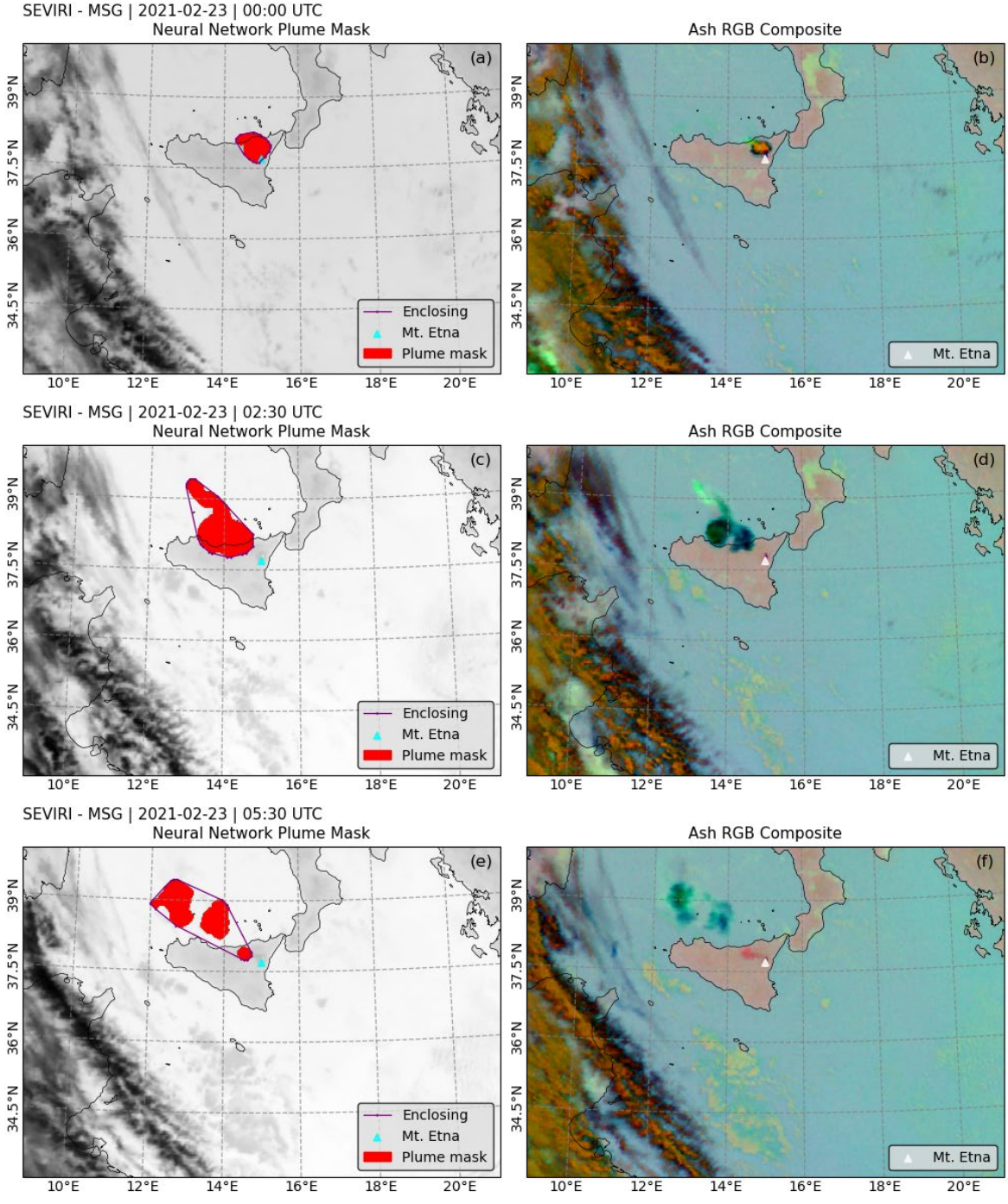

Figure 5. Sequence of SEVIRI images showing the evolution of the volcanic cloud from 22–23 February 2021. The left panel shows the plume mask (in red) generated by the Neural Network model, overlaid on the brightness temperature at 10.8 µm. In addition, a purple outline encloses the detected volcanic cloud. The right panel shows the standard Ash RGB composite. In all images, Mount Etna's location is marked with a white triangle. (a)–(b) correspond to 00:00 UTC, (c)–(d) to 02:30 UTC, and (e)–(f) to 05:30 UTC. The full image sequence is provided in the supplementary materials (Video 1).

https://doi.org/10.5194/egusphere-2026-727
Preprint. Discussion started: 23 February 2026

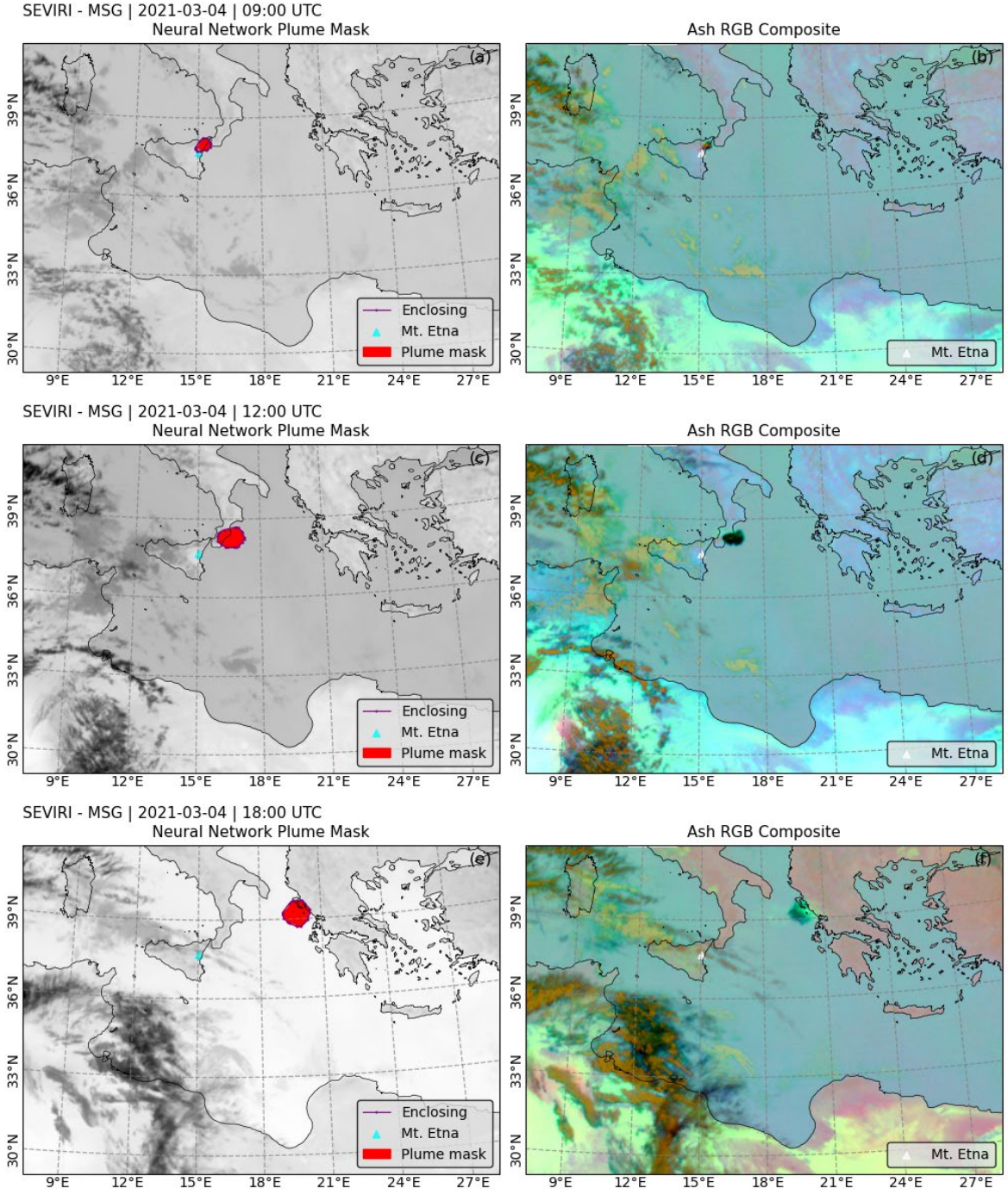

Figure 6. Sequence of SEVIRI images showing the evolution of the volcanic cloud from 04 Mar 2021. The left panel shows the plume mask (in red) generated by the Neural Network model, overlaid on the brightness temperature at 10.8 µm. In addition, a purple outline encloses the detected volcanic cloud. The right panel shows the standard Ash RGB composite. In all images, Mount Etna's location is marked with a white triangle. (a)–(b) correspond to 09:00 UTC, (c)–(d) to 12:00 UTC, and (e)–(f) to 18:00 UTC. The full image sequence is provided in the supplementary materials (Video 2).

https://doi.org/10.5194/egusphere-2026-727
Preprint. Discussion started: 23 February 2026

4.3. Event 3: 04 Aug 2024

This last validation event was also produced by a lava fountain, this time from the Voragine Crater, starting at 03:20 UTC. The fountain generated a volcanic cloud that rose to over 10 km (INGV, 2024). The volcanic cloud exhibited wind-driven behaviour, dispersing toward the east and southeast. This case is particularly challenging, as the volcanic cloud is composed of ash, ice, and SO_2, and is both surrounded and mixed with meteorological clouds.

At the onset, the volcanic cloud appears in red shades, with some SO_2 signal in green (see Figure 7b), before encountering the mid-level meteorological clouds. Note how the volcanic and meteorological clouds blend in Figure 7b and 7f. Detecting volcanic clouds under these conditions is generally very difficult as reported in previous studies (Prata et al., 2022; Taylor et al., 2023). Nevertheless the NN model successfully identified the volcanic cloud, and the tracking algorithm subsequently followed its evolution even when it was blended with meteorological clouds (see Figure 7a, 7c, and 7e). For this event, the obtained performance metrics were a precision of 0.89, a recall of 0.92 and a F1-score of 0.90 as reported in Table 5.

4.4. Metrics analyse

As can be seen in Table 5, the metrics indicate strong performance across all validation events. Looking at the precision and recall metrics, we can gain deeper insight into the performance of the NN model performance. For instance, the precision values for Event 1 and Event 2 are 96% and 98%, respectively, indicating that plenty of pixels detected as volcanic cloud were correctly classified. Whereas the recall values for Event 1 and Event 2 are 83% and 74%, respectively, indicating that the model was able to correctly identify that proportion of pixels when compared with the reference plume mask.

These relatively low recall values are likely due to dilution in the outer portions of the volcanic cloud, which fall below the detection limit of our NN model, although they remain visible to a human operator in the images. This hypothesis was also proposed by Theys et al. (2013). The limitation in detecting the more dilute portions of the volcanic cloud was previously discussed in Sections 4.1 and 4.2, where the effect became evident toward the end of the sequence. This is expected, as dilution increases over time as the cloud disperses, resulting in more false negatives for the NN model.

In contrast, for Event 3, the behaviour of the precision and recall metrics is opposite to that observed in the previous events. In this case, the precision is lower at 89%, while the recall is significantly higher at 92%. In other words, the recall indicates that in Event 3, the NN model correctly detected 92% of the pixels identified in the manual plume mask. Furthermore, the precision reveals that, of all pixels classified as volcanic cloud, 89% were correctly identified.

These results may be attributed to the challenging nature of Event 3, in which the volcanic cloud is mixed with and surrounded by meteorological clouds. Under these circumstances, the human operator responsible for generating the manual plume mask may have faced difficulty in identifying the volcanic cloud and distinguishing it from meteorological clouds. Despite this complexity, the NN model successfully detected the volcanic cloud throughout the sequence (see the Video 3 in the supplementary materials).

https://doi.org/10.5194/egusphere-2026-727
Preprint. Discussion started: 23 February 2026

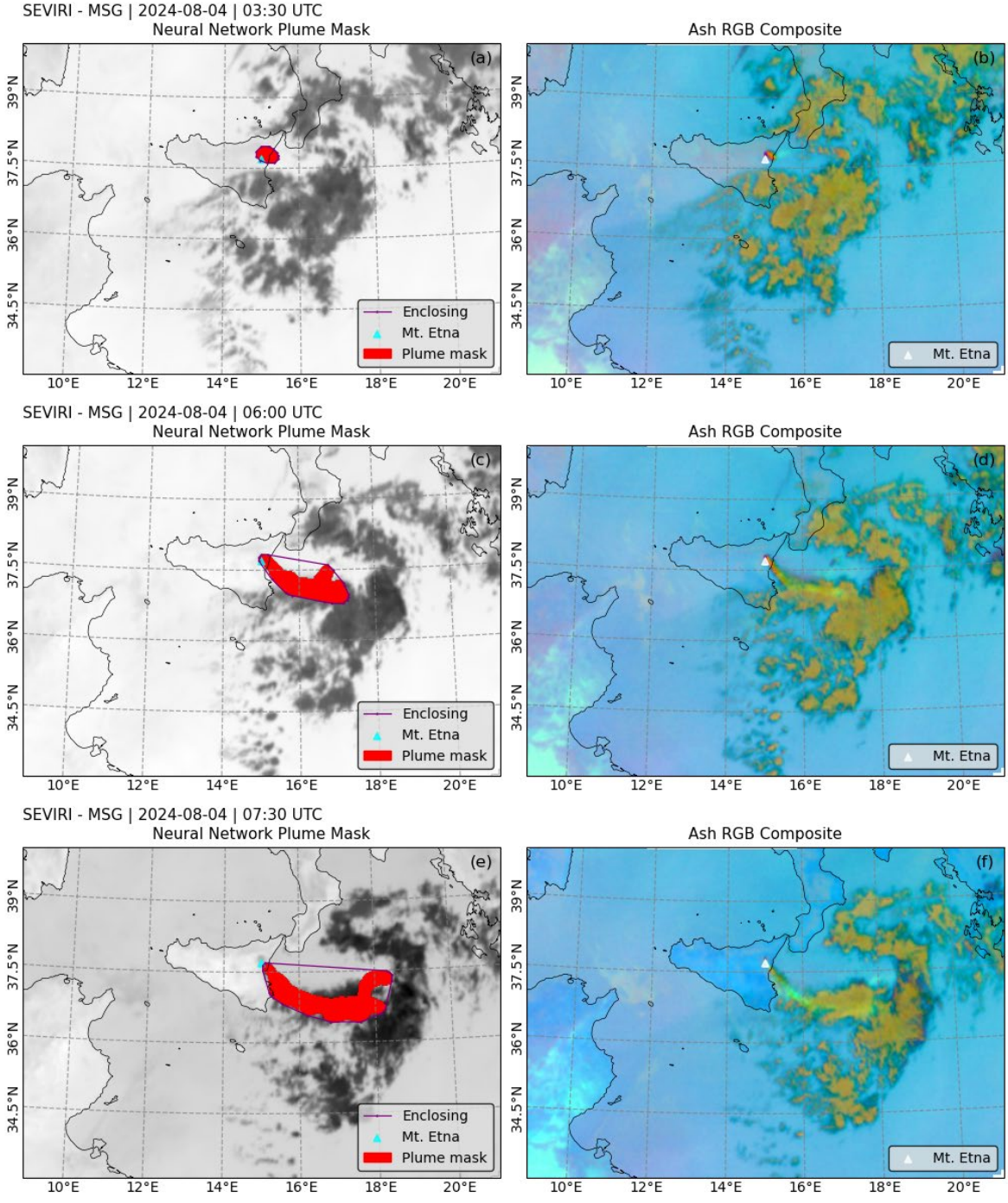

Figure 7. Sequence of SEVIRI images showing the evolution of the volcanic cloud from 04 Agu 2024. The left panel shows the plume mask (in red) generated by the Neural Network model, overlaid on the brightness temperature at 10.8 µm. In addition, a purple outline encloses the detected volcanic cloud. The right panel shows the standard Ash RGB composite. In all images, Mount Etna's location is marked with a white triangle. (a)–(b) correspond to 03:30 UTC, (c)–(d) to 06:00 UTC, and (e)–(f) to 07:30 UTC. The full image sequence is provided in the supplementary materials (Video 3).

https://doi.org/10.5194/egusphere-2026-727
Preprint. Discussion started: 23 February 2026

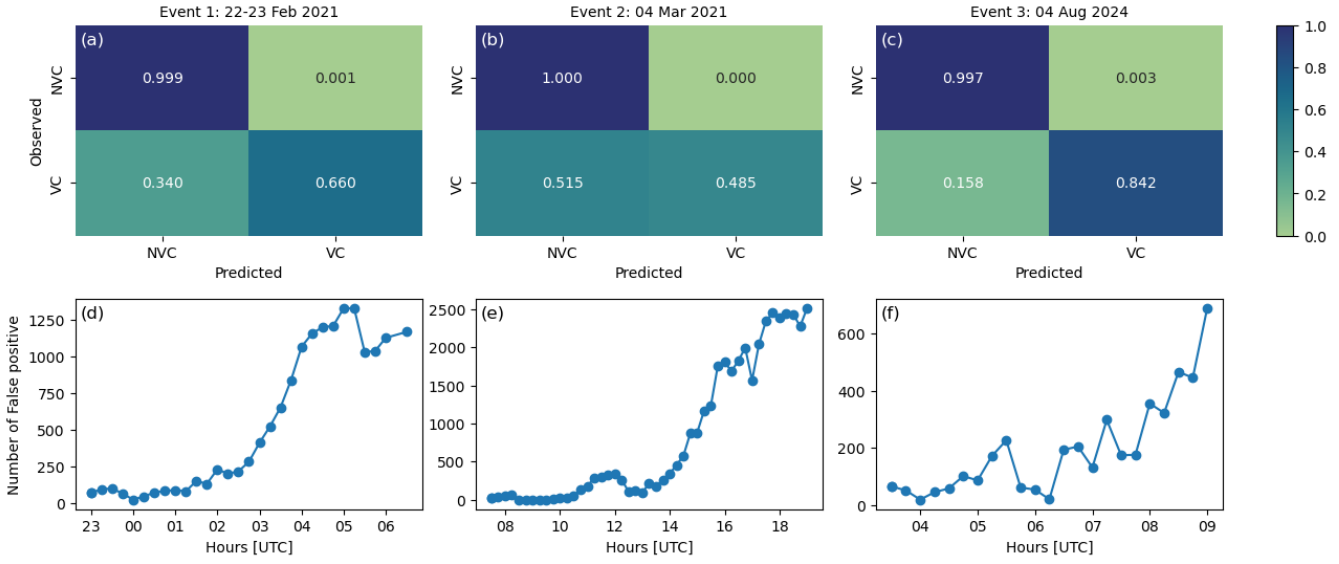

Figure 8. Confusion matrix and false positives number evolution for the validation events. (a) and (d) show the confusion matrix and false positives number evolution for the Event 1. (b) and (e) the same as the previous but for Event 2. (c) and (f) the same as the previous one but for Event 3.

The issue of the false positives, likely caused by the dilution of the volcanic cloud is evident when examining the confusion matrices for the complete images sequence for each event, shown in the Figure 8a-c. These confusion matrices are constructed using the predictions (detections) of the NN model and the observed (reference) plume mask (Fawcett, 2006). In Figure 8a-c the predictions are on the x-axis and the observation on the y-axis.

As previously discussed, the effect is more pronounced in the Event 1 and Event 2, which reach overall false positive rate of 34.0% and 51.5%, respectively, for the complete sequence. Meanwhile, for Event 3 the false positive rate is 15.8%. The question arises as to how the most challenging event achieved a lower false positive rate. We suggest that the answer lies in the generation of the manual plume mask. When the volcanic cloud is difficult to distinguish from meteorological clouds, the reference plume mask tends to be smaller and may not extend to the more dilute portions of the cloud. This situation reveals not only the potential of the NN model but also the limitations of the human operator under challenging conditions.

Furthermore, as illustrated in Figure 8d–f, the number of false positives progressively increases over time, consistent with expectations. Full animations illustrating the model's performance over the complete sequence are provided in the supplementary materials, including one animation for each validation event. These animations allow spatial visualization of true positives, false negatives, and false positives.

https://doi.org/10.5194/egusphere-2026-727
Preprint. Discussion started: 23 February 2026

5. Discussion

The aim of this work was to explore the detection of volcanic clouds containing a mixture of ash, ice, and SO_2, with a focus on leveraging Machine Learning techniques and data from the SEVIRI sensor. The results presented in the previous section demonstrate that the Neural Network model is capable of detecting volcanic clouds under challenging conditions, achieving high performance metrics, as shown in Table 5. These findings contrast with previous studies (Gupta et al., 2022; Prata et al., 2020; Rose et al., 1995; Taylor et al., 2023), where traditional methods failed to detect volcanic clouds in the presence of ice or water droplets. Therefore, our results provide compelling evidence that Machine Learning techniques enable the detection of volcanic clouds even in challenging scenarios.

To assess the impact of false negatives in the NN model detections, an additional analysis was conducted to estimate the volcanic cloud mass loading. The mass loading was retrieved using the Volcanic Plume Removal (VPR) algorithm (Pugnaghi et al., 2013, 2016), with the NN detection used as input. The resulting retrievals were then compared with those obtained from the manual plume mask and reported in Guerrieri et al. (2023). The results are presented in Figure 9, where the left panel shows the comparison of mass loading of ash, SO_2, and ice for Event 1, the central panel for Event 2, and the right panel for Event 3.

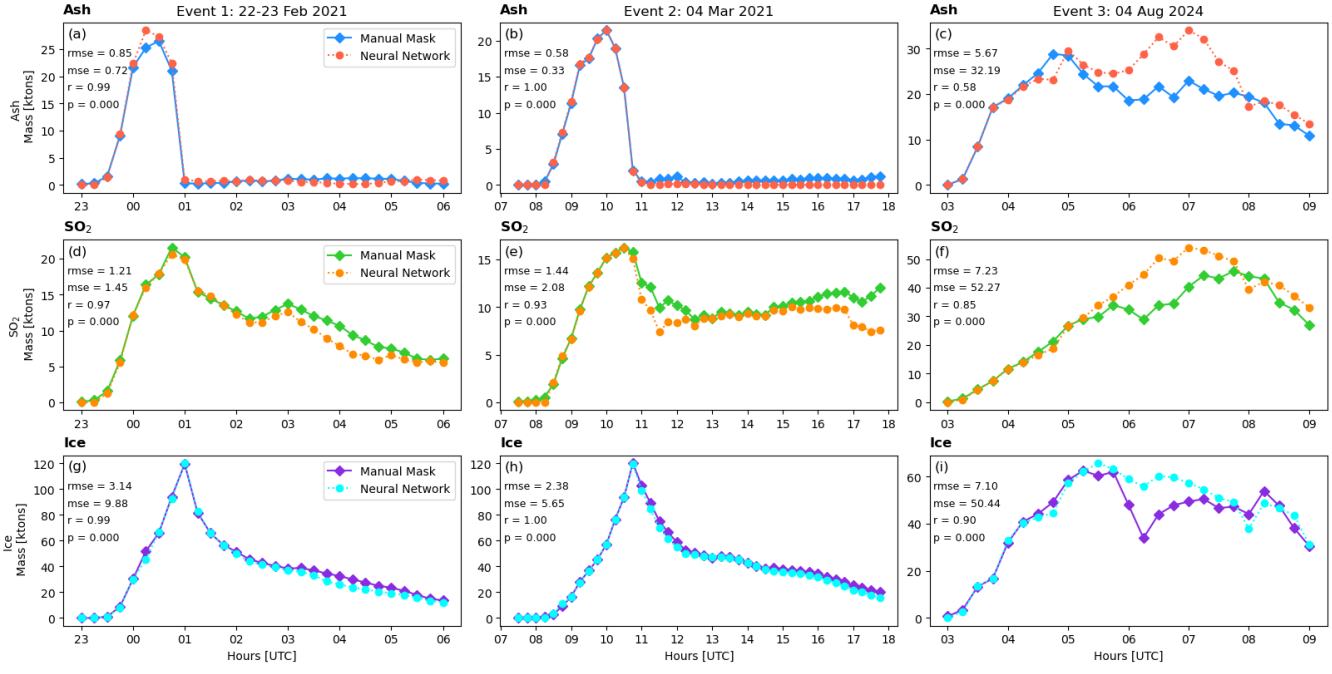

*RMSE and MSE are expressed in ktons.

Figure 9. Comparison of mass loading derived from the Neural Network detection and the manual plume mask. The left panel shows the mass loading evolution of ash, SO_2, and ice for Event 1 (22-23 February 2021). The central panel presents the same analysis for Event 2 (4 March 2021), and the right panel for Event 3 (4 August 2024). Error and correlation metrics between the two estimations are also reported.

https://doi.org/10.5194/egusphere-2026-727
Preprint. Discussion started: 23 February 2026

As can be seen in Figure 9, the evolution of ash, SO_2, and ice mass loading derived from the NN detection is in exceptionally good agreement with that obtained from the manual plume mask. Note that, in all retrievals presented in Figure 9, the largest differences occur in the middle or final stages of the sequence, coinciding with an increase in false positives rates (see Figure 8d–f). Nevertheless, the influence of false positive rates on the mass loading estimation appears to be minimal, as indicated by the generally strong correlation and low error values. Event 3 again exhibits the largest differences, likely due to its challenging nature and the difficulty faced by the human operator in discriminating the volcanic cloud from meteorological clouds during the generation of the plume mask. The quantitative comparison supports the hypothesis that the regions missed by the NN model correspond to the most diluted portions of the volcanic cloud, which apparently do not contribute significantly to the overall mass loading estimation.

The performance achieved by the NN model in the validation events is likely attributable to the integration of all 13 input features, including the full set of thermal-infrared channels (6–14 µm), and the ability of machine learning models to exploit multiple inputs to learn relevant multivariate relationships. Thus, to provide insight into the NN model's internal mechanisms, Figure 6 presents the feature relevance ranked according to their mean absolute SHAP values.

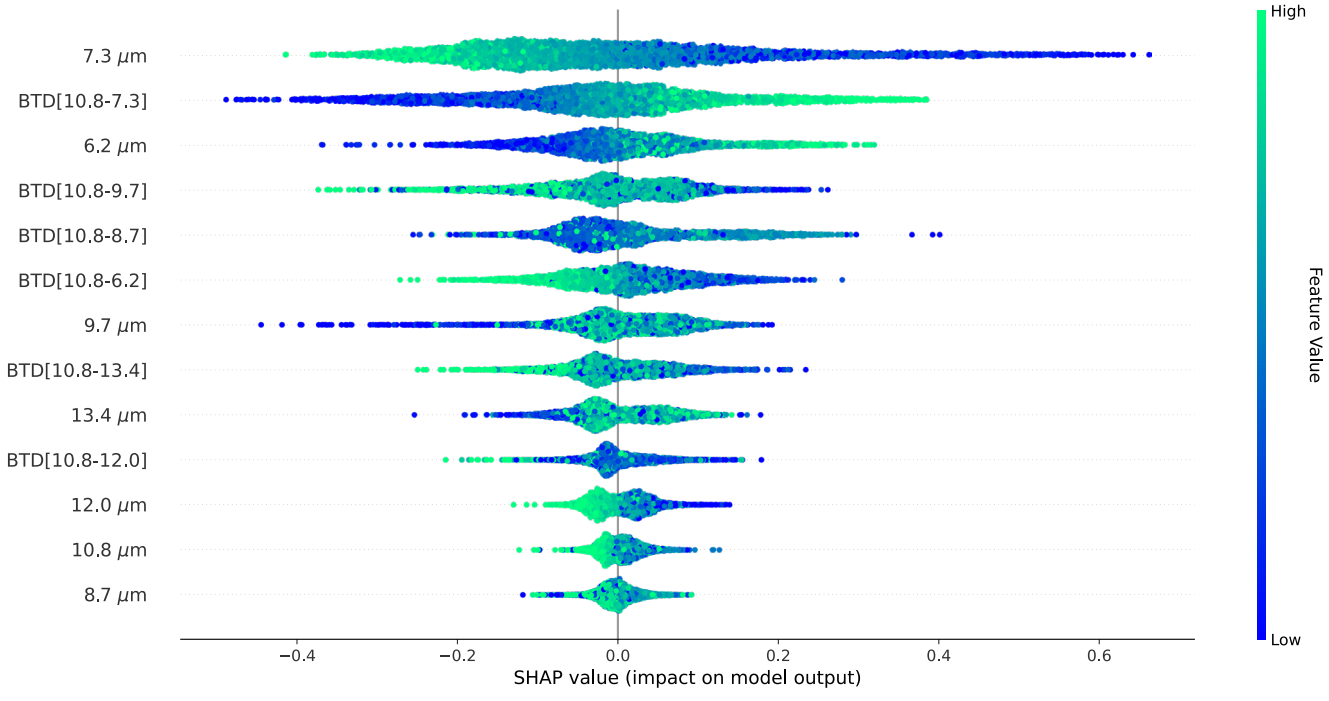

Figure 10. Feature relevance plot for the 13 features present in the volcanic cloud detection dataset. Scatter points are SHAP values, while the color coding indicates the minimum-maximum normalized value for each feature.

https://doi.org/10.5194/egusphere-2026-727
Preprint. Discussion started: 23 February 2026

According to Figure 6, it is interesting to note that the most relevant feature is the brightness temperature at 7.3 µm channel, followed by the BTD[10.8-7.3], and then the 6.2 µm channel. The 7.3 µm and 6.2 µm channels are known as the lower-level water vapour and the upper-level water vapour, respectively. Also, they are used to identify and track atmospheric elements (Schmit and Gunshor, 2020). The high relevance attributed to the 7.3 µm channel is likely due to the strong SO_2 absorption occurring at this wavelength (Pavolonis et al., 2020).

Following in the feature relevance ranking, BTD[10.8-9.7] and BTD[10.8-8.7] appear in fourth and fifth place, respectively. The BTD[10.8-12.0], widely recognized as the standard method for volcanic cloud detection ranks tenth, being surpassed even by the 13.3 µm channel. This result is expected given the well-known limitations of the BTD[10.8-12.0] method in detecting volcanic clouds under the challenging conditions investigated in this study.

The SHAP value distributions for each feature in Figure 10 also help to explain how the model operates. For instance, at the 7.3 µm channel, the SHAP values indicate that lower temperatures contribute to a positive detection of volcanic clouds, whereas higher temperatures contribute to a negative detection. This is expected because in the presence of SO_2, the 7.3 µm channel is affected by absorption, resulting in a lower reported temperature.

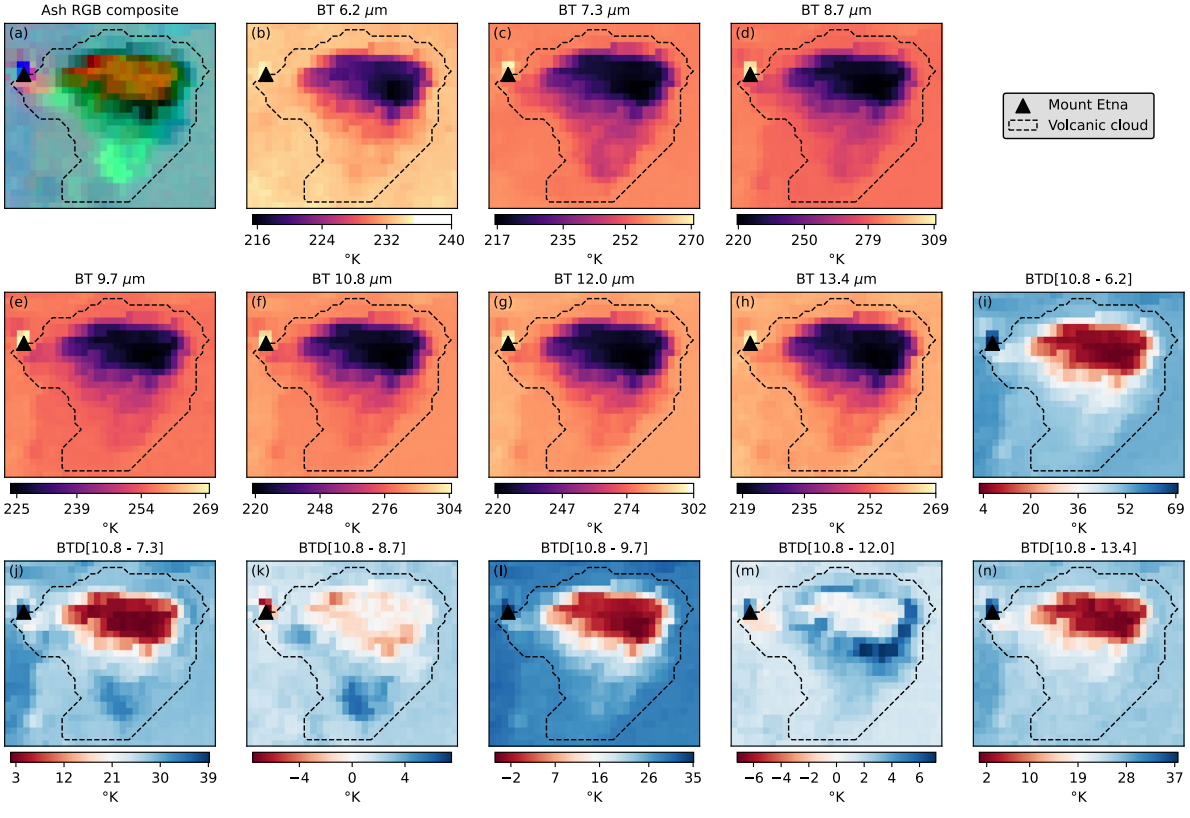

Figure 11. Zoom in on the volcanic cloud from 19 February 2021, as shown in Figure 1. Panel (a) displays the Ash RGB composite (same as Figure 1(b)), while panels (b)–(n) present all the features used during model training phase. Also shown is an overlaid hand-drawn volcanic cloud boundary, created during the labelling process.

https://doi.org/10.5194/egusphere-2026-727
Preprint. Discussion started: 23 February 2026

To complement the results provided by the SHAP values in Figure 10, Figure 11 displays a zoom in on the volcanic cloud from 19 February 2021, as shown in Figure 1. Panel (a) displays the Ash RGB composite (same as Figure 1b), while panels (b) through (n) present all the features. The information presented in Figures 7b-n, together with the feature relevance shown in Figure 10, provides insight into the relationships learned by the NN model.

The behavior of the 7.3 µm channel, as indicated by the SHAP values, is confirmed in Figure 11c, where lower brightness temperature values at the 7.3 µm channel are shown to align closely with the spatial extent of the volcanic cloud. Indeed, among all the features, the 7.3 µm channel most effectively represents the volcanic cloud in that case.

The limitation of the BTD[10.8-12.0] is evident in Figure 7m, where most of the volcanic cloud corresponds to BTD values around 0.0. This is expected, given that the presence of ice in volcanic clouds can compromise the performance of the BTD method.

6. Conclusions

We presented a Neural Network model to detect volcanic clouds containing a mixture of ash, ice, and SO_2 using data from the SEVIRI sensor onboard the geostationary satellite Meteosat-11. This study also described the generation of a training dataset, based on manual plume masks from more than 1.200 SEVIRI images. The result was a balanced binary training dataset comprising more than 2.200.000 pixels, with 13 features corresponding to seven thermal infrared bands and six BTDs. Furthermore, a tracking algorithm was proposed to improve the performance of the NN model.

The volcanic cloud detection produced by the NN model achieved an accuracy of 99%, along with very good precision (>89%) and recall (>74%) across the three validation events analysed. The integration of the NN model with the proposed plume tracking method enabled the tracking of the volcanic cloud across the image sequences for up to 12 hours. This strong performance demonstrates the ability of Machine Learning models to leverage multiple input features and learn complex multivariate relationships to address challenging detection problems, such as volcanic clouds in complex scenarios involving mixtures of ash, ice, and SO_2. In summary, this work shows that it is possible to automatically detect volcanic clouds in such complex scenarios.

However, the NN model shows limitations in detecting more diluted portions of the volcanic clouds, likely due to insufficient representation of such cases in the training dataset or because the signal falls below the sensor's detection limit. This limitation becomes evident when analysing the false positive rate, which increases during the middle and final parts of the image sequences. Nevertheless, we demonstrated that the false positives generated by the dilution process do not significantly affect the mass loading estimation. However, the inability to detect these diluted portions may have implications for aviation safety. Future work should focus on this limitation to determinate whether reliable detection of diluted cloud regions is feasible. Overall, the results are encouraging and provide valuable insight into the development of a near-real-time and automatic detection system for volcanic clouds, which is highly desirable for aviation safety.

https://doi.org/10.5194/egusphere-2026-727
Preprint. Discussion started: 23 February 2026

Data availability

All data used in this study are accessible through the EUMETCast Data Store. The trained neural network model and the constructed database are available from the authors upon reasonable request.

Author contributions

Writing (original draft preparation): CN. Conceptualization: CN and SC. Data curation: CN, LG, LM, DS. Formal Analysis: CN, SC and LG. Methodology: CN and MP. Project Software: CN. Supervision: SC and MP. Visualization: CN. Writing (review and editing): All authors.

Competing interests Data availability

Authors declare no competing interests related to this work.

Disclaimer

Copernicus Publications remains neutral with regard to jurisdictional claims made in the text, published maps, institutional affiliations, or any other geographical representation in this paper. While Copernicus Publications makes every effort to include appropriate place names, the final responsibility lies with the authors. Views expressed in the text are those of the authors and do not necessarily reflect the views of the publisher.

Acknowledgements

This work contains modified EUMETSAT Meteosat-10 and Meteosat-11 SEVIRI Level 1.5 data, acquired via EUMETCast Europe [2020, 2021, 2022, 2024].

Financial support

This research was partially supported by the ESA GET-IT project.

References

Alexander, D.: Volcanic ash in the atmosphere and risks for civil aviation: A study in European crisis management, International Journal of Disaster Risk Science, 4, 9–19, https://doi.org/10.1007/S13753-013-0003-0/METRICS, 2013.

Atkinson, P. M. and Tatnall, A. R. L.: Introduction Neural networks in remote sensing, http://dx.doi.org/10.1080/014311697218700, 18, 699–709, https://doi.org/10.1080/014311697218700, 1997.

https://doi.org/10.5194/egusphere-2026-727
Preprint. Discussion started: 23 February 2026

Braga-Neto, U.: Fundamentals of Pattern Recognition and Machine Learning, Fundamentals of Pattern Recognition and Machine Learning, 1–357, https://doi.org/10.1007/978-3-030-27656-0/COVER, 2020.

Bröcker, J. and Smith, L. A.: Increasing the Reliability of Reliability Diagrams, Weather Forecast., 22, 651–661, https://doi.org/10.1175/WAF993.1, 2007.

Buades, A., Coll, B., and Morel, J. M.: A non-local algorithm for image denoising, Proceedings - 2005 IEEE Computer Society Conference on Computer Vision and Pattern Recognition, CVPR 2005, II, 60–65, https://doi.org/10.1109/CVPR.2005.38, 2005.

Calvari, S. and Nunnari, G.: Comparison between Automated and Manual Detection of Lava Fountains from Fixed Monitoring Thermal Cameras at Etna Volcano, Italy, Remote Sensing 2022, Vol. 14, Page 2392, 14, 2392, https://doi.org/10.3390/RS14102392, 2022.

Corradini, S., Spinetti, C., Carboni, E., Tirelli, C., Buongiorno, M. F., Pugnaghi, S., and Gangale, G.: Mt. Etna tropospheric ash retrieval and sensitivity analysis using Moderate Resolution Imaging Spectroradiometer measurements, https://doi.org/10.1117/1.3046674, 2, 023550, https://doi.org/10.1117/1.3046674, 2008.

Corradini, S., Merucci, L., and Prata, A. J.: Retrieval of SO2 from thermal infrared satellite measurements: Correction procedures for the effects of volcanic ash, Atmos. Meas. Tech., 2, 177–191, https://doi.org/10.5194/AMT-2-177-2009, 2009.

Durant, A. J., Shaw, R. A., Rose, W. I., Mi, Y., and Ernst, G. G. J.: Ice nucleation and overseeding of ice in volcanic clouds, Journal of Geophysical Research: Atmospheres, 113, 9206, https://doi.org/10.1029/2007JD009064, 2008.

Ellrod, G. P., Connell, B. H., and Hillger, D. W.: Improved detection of airborne volcanic ash using multispectral infrared satellite data, Journal of Geophysical Research: Atmospheres, 108, 4356, https://doi.org/10.1029/2002JD002802, 2003.

Ash RGB Quick Guide | EUMETSAT - User Portal: https://user.eumetsat.int/resources/user-guides/ash-rgb-quick-guide, last access: 4 March 2025.

EUMETSAT: MSG Level 1.5 Image Data Format Description, EUM/MSG/ICD/105, 2017.

Fawcett, T.: An introduction to ROC analysis, Pattern Recognit. Lett., 27, 861–874, https://doi.org/10.1016/J.PATREC.2005.10.010, 2006.

Flora, M. L., Potvin, C. K., McGovern, A., and Handler, S.: A Machine Learning Explainability Tutorial for Atmospheric Sciences, Artificial Intelligence for the Earth Systems, 3, https://doi.org/10.1175/AIES-D-23-0018.1, 2024.

Gray, T. M. and Bennartz, R.: Automatic volcanic ash detection from MODIS observations using a back-propagation neural network, Atmos. Meas. Tech., 8, 5089–5097, https://doi.org/10.5194/AMT-8-5089-2015, 2015.

Guerrieri, L., Corradini, S., Theys, N., Stelitano, D., and Merucci, L.: Volcanic Clouds Characterization of the 2020–2022 Sequence of Mt. Etna Lava Fountains Using MSG-SEVIRI and Products' Cross-Comparison, Remote Sens. (Basel)., 15, 2055, https://doi.org/10.3390/RS15082055/S1, 2023.

Gupta, A. K., Bennartz, R., Fauria, K. E., and Mittal, T.: Eruption chronology of the December 2021 to January 2022 Hunga Tonga-Hunga Ha'apai eruption sequence, Communications Earth & Environment 2022 3:1, 3, 1–10, https://doi.org/10.1038/s43247-022-00606-3, 2022.

https://doi.org/10.5194/egusphere-2026-727
Preprint. Discussion started: 23 February 2026

Hillger, D. W. and Clark, J. D.: Principal Component Image Analysis of MODIS for Volcanic Ash. Part I: Most Important Bands and Implications for Future GOES Imagers, Journal of Applied Meteorology, 41, 985–1001, https://doi.org/https://doi.org/10.1175/1520-0450(2002)041<0985:PCIAOM>2.0.CO;2, 2002.

INGV: ETNA Bollettino Settimanale 01/03/2021 - 07/03/2021. Rep. N° 10/2021, 1–16 pp., 2021a.

INGV: ETNA Bollettino Settimanale 22/02/2021 - 28/02/2021. Rep. N° 09/2021, 1–15 pp., 2021b.

INGV: ETNA Bollettino Settimanale 29/07/2024 - 04/08/2024. Rep. N. 32/2024, 2024.

International Civil Aviation Organization (ICAO): Roadmap for International Airways Volcano Watch (IAVW) in Support of International Air Navigation, 2021.

International Civil Aviation Organization (ICAO): Quantitative Volcanic Ash (QVA) Concentration Information, 5 pp., 2024.

Jenkins, S., Smith, C., Allen, M., and Grainger, R.: Tonga eruption increases chance of temporary surface temperature anomaly above 1.5 °C, Nat. Clim. Chang., 13, 127–129, https://doi.org/10.1038/S41558-022-01568-2;SUBJMETA=106,1108,2786,674,694,704;KWRD=ATTRIBUTION,CLIMATE+AND+EARTH+SYSTEM+MODELLING,PROJECTION+AND+PREDICTION, 2023.

Kingma, D. P. and Ba, J. L.: Adam: A Method for Stochastic Optimization, 3rd International Conference on Learning Representations, ICLR 2015 - Conference Track Proceedings, 2014.

Lundberg, S. M., Allen, P. G., and Lee, S.-I.: A Unified Approach to Interpreting Model Predictions, 31st Conference on Neural Information Processing Systems (NIPS), https://doi.org/10.5555/3295222.3295230, 2017.

Marshall, L. R., Maters, E. C., Schmidt, A., Timmreck, C., Robock, A., and Toohey, M.: Volcanic effects on climate: recent advances and future avenues, Bulletin of Volcanology 2022 84:5, 84, 1–14, https://doi.org/10.1007/S00445-022-01559-3, 2022.

Mayberry, G. C., Rose, W. I., and Bluth, G. J. S.: Dynamics of volcanic and meteorological clouds produced on 26 December (Boxing Day) 1997 at Soufrière Hills Volcano, Montserrat, Geological Society Memoir, 21, 539–556, https://doi.org/10.1144/GSL.MEM.2002.021.01.24, 2002.

Ojala, M. and Garriga, G. C.: Permutation Tests for Studying Classifier Performance, Journal of Machine Learning Research, 11, 1833–1863, 2010.

Pardini, F., Barsotti, S., Bonadonna, C., Vitturi, M. de' M., Folch, A., Mastin, L., Osores, S., and Prata, A. T.: Dynamics, Monitoring, and Forecasting of Tephra in the Atmosphere, Reviews of Geophysics, 62, e2023RG000808, https://doi.org/10.1029/2023RG000808, 2024.

Pavolonis, M. J., Feltz, W. F., Heidinger, A. K., and Gallina, G. M.: A Daytime Complement to the Reverse Absorption Technique for Improved Automated Detection of Volcanic Ash, J. Atmos. Ocean. Technol., 23, 1422–1444, https://doi.org/10.1175/JTECH1926.1, 2006.

Pavolonis, M. J., Sieglaff, J., and Cintineo, J.: Spectrally Enhanced Cloud Objects—A generalized framework for automated detection of volcanic ash and dust clouds using passive satellite measurements: 1. Multispectral analysis, Journal of Geophysical Research: Atmospheres, 120, 7813–7841, https://doi.org/10.1002/2014JD022968, 2015a.

https://doi.org/10.5194/egusphere-2026-727
Preprint. Discussion started: 23 February 2026

Pavolonis, M. J., Sieglaff, J., and Cintineo, J.: Spectrally Enhanced Cloud Objects—A generalized framework for automated detection of volcanic ash and dust clouds using passive satellite measurements: 2. Cloud object analysis and global application, Journal of Geophysical Research: Atmospheres, 120, 7842–7870, https://doi.org/10.1002/2014JD022969, 2015b.

Pavolonis, M. J., Sieglaff, J., and Cintineo, J.: Automated Detection of Explosive Volcanic Eruptions Using Satellite-Derived Cloud Vertical Growth Rates, Earth and Space Science, 5, 903–928, https://doi.org/10.1029/2018EA000410;PAGEGROUP:STRING:PUBLICATION, 2018.

Pavolonis, M. J., Sieglaff, J. M., and Cintineo, J. L.: Remote Sensing of Volcanic Ash with the GOES-R Series, The GOES-R Series: A New Generation of Geostationary Environmental Satellites, 103–124, https://doi.org/10.1016/B978-0-12-814327-8.00010-X, 2020.

Pergola, N., Tramutoli, V., Marchese, F., Scaffidi, I., and Lacava, T.: Improving volcanic ash cloud detection by a robust satellite technique, Remote Sens. Environ., 90, 1–22, https://doi.org/10.1016/J.RSE.2003.11.014, 2004.

Petracca, I., De Santis, D., Picchiani, M., Corradini, S., Guerrieri, L., Prata, F., Merucci, L., Stelitano, D., Del Frate, F., Salvucci, G., and Schiavon, G.: Volcanic cloud detection using Sentinel-3 satellite data by means of neural networks: the Raikoke 2019 eruption test case, Atmos. Meas. Tech., 15, 7195–7210, https://doi.org/10.5194/AMT-15-7195-2022, 2022.

Picchiani, M., Chini, M., Corradini, S., Merucci, L., Sellitto, P., Del Frate, F., and Stramondo, S.: Volcanic ash detection and retrievals using MODIS data by means of neural networks, Atmos. Meas. Tech., 4, 2619–2631, https://doi.org/10.5194/amt-4-2619-2011, 2011.

Picchiani, M., Chini, M., Corradini, S., Merucci, L., Piscini, A., and Frate, F. Del: Neural network multispectral satellite images classification of volcanic ash plumes in a cloudy scenario, Annals of Geophysics, 57, https://doi.org/10.4401/ag-6638, 2015.

Piscini, A., Picchiani, M., Chini, M., Corradini, S., Merucci, L., Del Frate, F., and Stramondo, S.: A neural network approach for the simultaneous retrieval of volcanic ash parameters and SO2 using MODIS data, Atmos. Meas. Tech., 7, 4023–4047, https://doi.org/10.5194/amt-7-4023-2014, 2014.

Prata, A. J.: Infrared radiative transfer calculations for volcanic ash clouds, Geophys. Res. Lett., 16, 1293–1296, https://doi.org/10.1029/GL016i011p01293, 1989a.

Prata, A. J.: Observations of Volcanic Ash Clouds in the 10-12 micrometers window using AVHRR-2 data.pdf, 1989b.

Prata, A. T., Folch, A., Prata, A. J., Biondi, R., Brenot, H., Cimarelli, C., Corradini, S., Lapierre, J., and Costa, A.: Anak Krakatau triggers volcanic freezer in the upper troposphere, Scientific Reports 2020 10:1, 10, 1–13, https://doi.org/10.1038/s41598-020-60465-w, 2020.

Prata, A. T., Grainger, R. G., Taylor, I. A., Povey, A. C., Proud, S. R., and Poulsen, C. A.: Uncertainty-bounded estimates of ash cloud properties using the ORAC algorithm: Application to the 2019 Raikoke eruption, Atmos. Meas. Tech., 15, 5985–6010, https://doi.org/10.5194/AMT-15-5985-2022, 2022.

Prata, F. and Rose, B.: Volcanic Ash Hazards to Aviation, The Encyclopedia of Volcanoes, 911–934, https://doi.org/10.1016/B978-0-12-385938-9.00052-3, 2015.

https://doi.org/10.5194/egusphere-2026-727
Preprint. Discussion started: 23 February 2026

Prata, F., Bluth, G., Rose, B., Schneider, D., and Tupper, A.: Comments on "Failures in detecting volcanic ash from a satellite-based technique," Remote Sens. Environ., 78, 341–346, https://doi.org/10.1016/S0034-4257(01)00231-0, 2001.

Pugnaghi, S., Guerrieri, L., Corradini, S., Merucci, L., and Arvani, B.: A new simplified approach for simultaneous retrieval of SO2 and ash content of tropospheric volcanic clouds: an application to the Mt Etna volcano, Atmos. Meas. Tech., 6, 1315–1327, https://doi.org/10.5194/amt-6-1315-2013, 2013.

Pugnaghi, S., Guerrieri, L., Corradini, S., and Merucci, L.: Real time retrieval of volcanic cloud particles and SO2 by satellite using an improved simplified approach, Atmos. Meas. Tech., 9, 3053–3062, https://doi.org/10.5194/AMT-9-3053-2016, 2016.

Rainio, O., Teuho, J., and Klén, R.: Evaluation metrics and statistical tests for machine learning, Sci. Rep., 14, 1–14, https://doi.org/10.1038/S41598-024-56706-X;SUBJMETA=117,531,639,705;KWRD=COMPUTER+SCIENCE,STATISTICS, 2024.

Romeo, F., Mereu, L., Scollo, S., Papa, M., Corradini, S., Merucci, L., and Marzano, F. S.: Volcanic Cloud Detection and Retrieval Using Satellite Multisensor Observations, Remote Sensing 2023, Vol. 15, Page 888, 15, 888, https://doi.org/10.3390/RS15040888, 2023.

Rose, W. I., Delene, D. J., Schneider, D. J., Bluth, G. J. S., Krueger, A. J., Sprod, I., McKee, C., Davies, H. L., and Ernst, G. G. J.: Ice in the 1994 Rabaul eruption cloud: implications for volcano hazard and atmospheric effects, Nature 1995 375:6531, 375, 477–479, https://doi.org/10.1038/375477a0, 1995.

Rose, W. I., Gu, Y., Watson, I. M., Yu, T., Bluth, G. J. S., Prata, A. J., Krueger, A. J., Krotkov, N. A., Carn, S., Fromm, M. D., Hunton, D. E., Ernst, G. G. J., Viggiano, A. A., Miller, T. M., Ballenthin, J. O., Reeves, J. M., Wilson, J. C., Anderson, B. E., and Flittner, E.: The February–March 2000 Eruption of Hekla, Iceland from a Satellite Perspective, Geophysical Monograph Series, 139, 107–132, https://doi.org/10.1029/139GM07, 2003.

Schill, G. P., Genareau, K., and Tolbert, M. A.: Deposition and immersion-mode nucleation of ice by three distinct samples of volcanic ash, Atmos. Chem. Phys., 15, 7523–7536, https://doi.org/10.5194/ACP-15-7523-2015, 2015.

Schmit, T. J. and Gunshor, M. M.: ABI Imagery from the GOES-R Series, The GOES-R Series: A New Generation of Geostationary Environmental Satellites, 23–34, https://doi.org/10.1016/B978-0-12-814327-8.00004-4, 2020.

Seifert, P., Ansmann, A., Groß, S., Freudenthaler, V., Heinold, B., Hiebsch, A., Mattis, I., Schmidt, J., Schnell, F., Tesche, M., Wandinger, U., and Wiegner, M.: Ice formation in ash-influenced clouds after the eruption of the Eyjafjallajökull volcano in April 2010, Journal of Geophysical Research: Atmospheres, 116, 0–04, https://doi.org/10.1029/2011JD015702, 2011.

Stelitano, D., Merucci, L., Ficeli, P., and Zanolin, F.: Satellite Acquisition System at INGV Rome headquarters, Rome, 2023.

Stewart, C., Damby, D. E., Horwell, C. J., Elias, T., Ilyinskaya, E., Tomašek, I., Longo, B. M., Schmidt, A., Carlsen, H. K., Mason, E., Baxter, P. J., Cronin, S., and Witham, C.: Volcanic air pollution and human health: recent advances and future directions, Bulletin of Volcanology 2021 84:1, 84, 1–25, https://doi.org/10.1007/S00445-021-01513-9, 2021.

Taylor, I. A., Grainger, R. G., Prata, A. T., Proud, S. R., Mather, T. A., and Pyle, D. M.: A satellite chronology of plumes from the April 2021 eruption of La Soufrière, St Vincent, Atmos. Chem. Phys., 23, 15209–15234, https://doi.org/10.5194/ACP-23-15209-2023, 2023.

https://doi.org/10.5194/egusphere-2026-727
Preprint. Discussion started: 23 February 2026

Theys, N., Campion, R., Clarisse, L., Brenot, H., Van Gent, J., Dils, B., Corradini, S., Merucci, L., Coheur, P. F., Van Roozendael, M., Hurtmans, D., Clerbaux, C., Tait, S., and Ferrucci, F.: Volcanic SO2 fluxes derived from satellite data: A survey using OMI, GOME-2, IASI and MODIS, Atmos. Chem. Phys., 13, 5945–5968, https://doi.org/10.5194/ACP-13-5945-2013, 2013.

Torrisi, F., Amato, E., Corradino, C., Mangiagli, S., and Del Negro, C.: Characterization of Volcanic Cloud Components Using Machine Learning Techniques and SEVIRI Infrared Images, Sensors 2022, Vol. 22, Page 7712, 22, 7712, https://doi.org/10.3390/S22207712, 2022.

Torrisi, F., Corradino, C., Cariello, S., and Del Negro, C.: Enhancing detection of volcanic ash clouds from space with convolutional neural networks, Journal of Volcanology and Geothermal Research, 448, 108046, https://doi.org/10.1016/J.JVOLGEORES.2024.108046, 2024.

Wang, P. K.: Physics and Dynamics of Clouds and Precipitation, Physics and Dynamics of Clouds and Precipitation, 9781107005563, 1–460, https://doi.org/10.1017/CBO9780511794285, 2013.

Yang, X.-S.: Neural networks and deep learning, Introduction to Algorithms for Data Mining and Machine Learning, 139–161, https://doi.org/10.1016/B978-0-12-817216-2.00015-6, 2019.

Yu, T., Rose, W. I., and Prata, A. J.: Atmospheric correction for satellite-based volcanic ash mapping and retrievals using "split window" IR data from GOES and AVHRR, Journal of Geophysical Research Atmospheres, 107, AAC 10-1-AAC 10-19, https://doi.org/10.1029/2001JD000706, 2002.